ChemComm

Accepted Manuscript

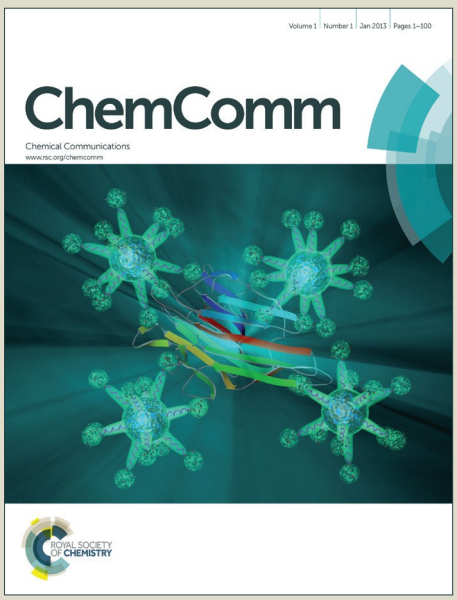

ROYAL SOCIETY OF CHEMISTRY

www.rsc.org/chemcomm

Journal Name

ARTICLE

FeP and FeP_2 Nanowires for Efficient Electrocatalytic Hydrogen Evolution Reaction†

Received 00th January 20xx,
Accepted 00th January 20xx

DOI: 10.1039/x0xx00000x

www.rsc.org/

Chang Yong Son, In Hye Kwak, Young Rok Lim and Jeunghee Park*

We report achieving efficient electrocatalytic hydrogen evolution reaction using composition-controlled iron phosphide (FeP and FeP_2) nanowires. The respective Tafel slopes of nanowire arrays were 39 and 37 mV dec^{-1} in 0.5 M H_2SO_4, and 75 and 67 mV dec^{-1} in 1 M KOH. The richer P composition produced excellent electrocatalytic efficiency.

Hydrogen generated from water splitting has great potential for use as a clean, recyclable, and relatively low-cost energy source. Over the past decade, fundamental progress has been made in developing novel catalyst materials for water-splitting reactions. However, constructing an efficient device capable of producing hydrogen at a scale and cost that can compete with fossil fuels remains a significant challenge. Currently, platinum (Pt) is state-of-art catalyst as only small overpotentials are required for high reaction rates. However, the scarcity and high cost of Pt may limit its widespread technological use. This limitation has motivated significant efforts toward replacing Pt with earth-abundant non-noble metal or metal-free materials.[1-8] Transition metal phosphides are one type of attractive semiconductor materials, which have a low band gap, making them electrically conductive, and exhibit good stability in acidic and basic media compared to their pure metal counterparts.[9-39]

Despite the remarkable hydrogen evolution reaction (HER) activity of metal phosphides used in water splitting, controlling the composition of these materials to increase their efficiency remains challenging, and only a few cases have been reported. Recently, Schaak's group reported that CoP exhibits better HER catalytic activity than Co_2P.[27] Additionally, a number of works have confirmed the higher HER efficiency of P-rich Ni_5P_4 nanostructures and the lower efficiency of P-deficient $Ni_{12}P_5$ compared to Ni_2P.[29-31] Motivated by these results, herein, we developed novel synthetic methods to produce FeP and FeP_2 nanowires (NWs) with two different morphologies; one is NW array directly grown on substrates and the other one is freestanding NWs. We demonstrated the relatively high electrocatalytic activity of P-rich FeP_2 NWs for HER in both acidic and basic media.

FeP and FeP_2 NW arrays were synthesized through the phosphidation reaction of pre-grown vertically aligned Fe_2O_3 NWs with phosphine (PH_3) gas. This method has many advantages, including high yield, short reaction time, and excellent reproducibility and requires no additional fabrication processes. The detailed experimental procedure is described in the Electronic Supplementary Information (ESI†).

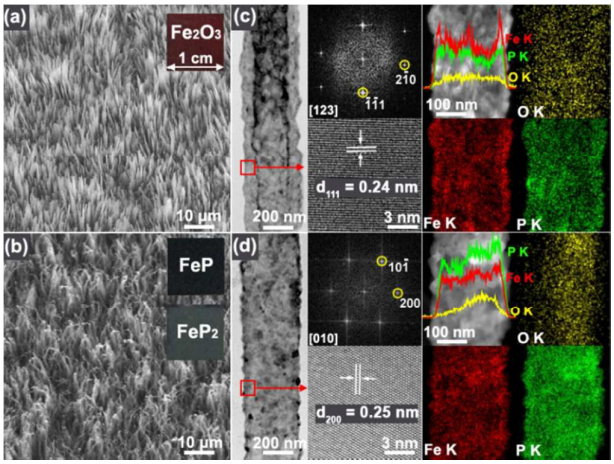

Fig. 1 SEM micrographs of (a) Fe_2O_3 and (b) FeP_2 NW arrays grown on substrates. Photographs show a red Fe_2O_3, a black FeP, and a grey FeP_2 NW arrays on a 1×1 cm^2 size Fe foil. HRTEM and corresponding FFT images of orthorhombic-phase (c) FeP and (d) FeP_2 NWs. EDX mapping and line-scan profiles of Fe K shell, P K shell, and O K shell showing the Fe_3O_4-FeP and Fe_3O_4-FeP_2 core-shell structures

Fig. 1a presents the SEM image of the vertically aligned Fe_2O_3 NWs. The photograph shows the homogenous growth of Fe_2O_3 NWs (red) over a large area of substrate (1×1 cm^2). These NWs were synthesized by oxidizing Fe foil, as described elsewhere.[40] The average length of these NWs is 10 μm. After the phosphidation reaction, red color (Fe_2O_3) becomes black (FeP) or grey (FeP_2). The

Department of Chemistry, Korea University, Jochiwon 339-700 (Korea)
E-mail: parkjh@korea.ac.kr.
† Electronic Supplementary Information (ESI) available: See DOI: 10.1039/x0xx00000x

SEM images and photographs show the homogenous growth of FeP and FeP_2 NWs over entire substrates (Fig. 1b). Control over the composition was achieved by varying the reaction temperature; 350 °C for FeP and 400 °C for FeP_2. X-ray diffraction (XRD) pattern analysis confirmed the orthorhombic phase of the FeP (JCPDS No. 78-1443, a = 5.193 Å, b = 3.099 Å, c = 5.792 Å) and FeP_2 (JCPDS No. 71-2234, a = 4.972 Å, b = 5.656 Å, c = 2.723 Å) NWs (see the ESI†, Fig. S1). Both samples contain the Fe_3O_4 phase, which was probably produced by the reduction of Fe_2O_3 under hydrogen-rich condition during the phosphidation reaction. We separately prepared the Fe_3O_4 NW array by the thermal reaction of as-grown Fe_2O_3 at 650 °C using hydrogen gas. The density of the as-grown FeP and FeP_2 NWs is measured to be *ca.* 60 and 45 mg cm^{-2}, respectively.

Fig. 1c presents the high-resolution transmission electron microscopy (HRTEM) and fast-Fourier transform (FFT) images of the FeP NWs. The average diameter is 250 nm. A rough surface was observed along the entire wire axis of the FeP NWs. The NW's edge has been magnified to reveal the polycrystalline structure. The lattice-resolved image of the single-crystalline domain shows that the *d*-spacing between the neighboring (111) planes (d_{111}) is 2.4 Å (at the zone axis of [123]), which is consistent with that of orthorhombic-phase FeP. Energy-dispersive X-ray fluorescence (EDX) mapping and the line-scan profile of Fe K shell, P K shell, and O K shell show that the atomic ratio of Fe and P is 1:1 in the outer region and that the oxygen is mainly distributed inside the NW, suggesting a Fe_3O_4-FeP core-shell structure.

The HRTEM and FFT images of the FeP_2 NWs are shown in Fig. 1d. The average diameter is 300 nm. Magnifying the image reveals the surface's polycrystalline nature. The *d*-spacing between the neighboring (200) planes (d_{200}) is 2.5 Å at the zone axis of [010], which is consistent with that of orthorhombic-phase FeP_2. EDX mapping and line-scan profiles reveal the Fe_3O_4 phase in the cores of the FeP_2 NWs. The Fe and P exist at an atomic ratio of 1:2 in the shell part of Fe_3O_4-FeP_2 core-shell structures.

To evaluate the electrocatalytic HER performance, we performed linear sweep voltammetry (LSV) using the as-grown NW arrays as the working electrode. A typical three-electrode setup was used (see the ESI† for experimental details). Table 1 summarizes the results.

Fig. 2a shows the LSV curves (with iR-corrected) for FeP and FeP_2 NWs in H_2-saturated 0.5 M H_2SO_4 solution (scan rate: 2 mV s^{-1}). The potentials reported here were referenced to the reversible hydrogen electrode (RHE) through standard calibration. The overpotential (η) is defined as the applied potential (E) vs. RHE. For reference, we also performed measurements using a commercial Pt/C catalyst (20 wt % Pt on Vulcan carbon black), exhibiting high HER catalytic performance (with a near-zero overpotential). The Pt/C (1 mg cm^{-2}) was deposited on a glassy carbon (GC) electrode, and the performance was examined at a rotation speed of 1600 rpm. The LSV curves of Fe_2O_3 and Fe_3O_4 NW array were measured, confirming no HER catalytic activity. The overpotentials needed to deliver 10 mA cm^{-2} current density were found to be 96, 61, and 15 mV for FeP, FeP_2, and Pt/C, respectively.

The catalysis kinetics for the HER was examined using Tafel plots based on the Tafel equation: $\eta = b \log(J/J_0)$ (Fig. 2b). The Tafel slope (b) and exchange current density (J_0) were obtained from the linear portion in the low-potential region, which corresponds to the activation-controlled current density region. The Tafel slopes are 39, 37, and 30 mV dec^{-1} (dec = decade) for FeP, FeP_2, and Pt/C, respectively. The respective exchange currents are 0.17, 0.55, and 3.23 mA cm^{-2}. The results confirm the higher catalytic activity of FeP_2 relative to FeP, which is consistent with the results obtained for CoP, CoP_2, $Ni_{12}P_5$, Ni_2P, and Ni_5P_4.[27,29-31]

Table 1 Experimental overpotential and Tafel plot parameters of FeP and FeP_2 NWs

Electrolyte	Sample	η (mV)[a]	b (mV dec^{-1})[b]	J_0 (mA cm^{-2})[c]
Acid: 0.5 M H_2SO_4	FeP array	96	39	0.17
	FeP_2 array	61	37	0.55
	FeP free[d]	193	66	0.039
	FeP_2 free	128	40	0.17
	Pt/C	15	30	3.23
Base: 1 M KOH	FeP array	194	75	0.035
	FeP_2 array	189	67	0.035
	FeP free	274	134	0.095
	FeP_2 free	253	100	0.032
	Pt/C	90	53	0.87

[a] Overpotential at J=10 mA cm^{-2}, [b,c] Parameters of the Tafel equation: $\eta = b \log(J/J_0)$, where η is the overpotential (measured), b is the Tafel slope (mV dec^{-1}), J is the current density (measured), and J_0 is the exchange current density (mA cm^{-2}); [d] Freestanding NWs.

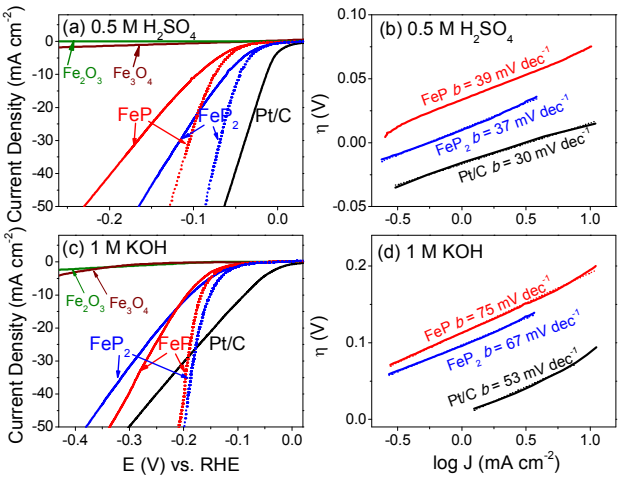

Fig. 2 LSV curves of the HER in (a) 0.5 M H_2SO_4 and (c) 1 M KOH for Fe_2O_3, Fe_3O_4, FeP, and FeP_2 NW arrays and a commercial Pt/C catalyst. (b), (d) Tafel plots derived from the LSV curves. Dotted lines show iR-corrected data for FeP and FeP_2.

The Tafel slope of 30 mV dec^{-1} for Pt/C indicates that the HER follows the Volmer-Tafel mechanism; $H_3O^+ + e^- \rightarrow H_{ads} + H_2O$ and $H_{ads} + H_{ads} \rightarrow H_2$ (b = 30 mV dec^{-1}). For FeP and FeP_2 NWs, the Volmer-Heyrovsky mechanism; $H_3O^+ + e^- \rightarrow H_{ads} + H_2O$ and $H_{ads} + H_3O^+ + e^- \rightarrow H_2 + H_2O$ (b = 40 mV dec^{-1}), is at work. The Tafel slope determined here is near the lowest value reported previously: 32 mV dec^{-1} measured for FeP nanoparticles on carbon cloth in 0.5 M H_2SO_4 by Sun's group.[15] Table S1 (see the ESI†) summarizes the previous works investigating FeP and FeP_2.

The electrocatalytic HER performance was also measured in 1 M

KOH, as shown in Fig. 2c. The overpotentials needed to deliver J = 10 mA cm^{-2} were found to be 194, 189, and 90 mV for FeP, FeP_2, and Pt/C, respectively. Correcting the raw data for iR losses revealed even more impressive performance of FeP_2 compared to that of FeP. The linear portions of the Tafel plots were fit to the Tafel equation, yielding Tafel slopes of 75, 67, and 53 mV dec^{-1} for FeP, FeP_2, and Pt/C, respectively (Fig. 2d). The slope values suggest that the HER follows the Volmer-Heyrovsky mechanism. The Tafel slopes are comparable to that reported for FeP nanotubes on carbon cloth: b = 59.5 mV dec^{-1}.[22]

The chronoamperometric response measurements confirm these materials' higher stability in base than in acid (see the ESI†, Fig. S2). The FeP_2 NWs are more stable than the FeP NWs, and current attenuations of 20 % and 12 % (at -0.2 V) within 8 h were observed in 1 M KOH for the FeP and FeP_2 NWs, respectively. X-ray photoelectron spectroscopy (XPS) data revealed the negligible degradation of FeP_2 NW during HER in 1 M KOH (Fig. S3, ESI†). The SEM images and XRD pattern confirmed that the morphology and phase of FeP_2 NWs are nearly unchanged. It suggests that the FeP_2 NWs are more competitive with the state-of-the-art HER catalysts than the FeP NWs, especially in basic medium.

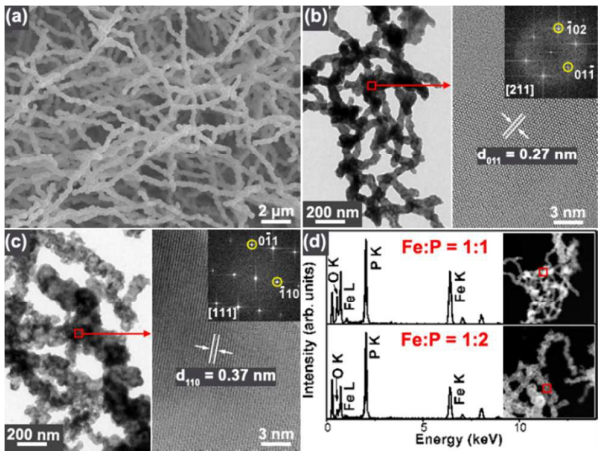

Fig. 3 (a) SEM micrographs and (b) HRTEM images of freestanding FeP NWs and (c) FeP_2 NWs. (d) EDX spectra of FeP and FeP_2 NWs, showing Fe:P= 1:1 and 1:2, respectively.

To support this result, we synthesized freestanding FeP and FeP_2 NWs containing no trace of the Fe_3O_4 phase (see the XRD data in the ESI†, Fig. S1) and examined their electrocatalytic efficiency. The NWs were synthesized via a thermal reaction of pre-grown Fe NWs (synthesized by filament-assisted thermal decomposition of $Fe(CO)_5$) with PH_3. SEM image showed a chain-like wire morphology (Fig. 3a). HRTEM and FFT images revealed that the single-crystalline FeP nanocrystals aggregate to form the wire (Fig. 3b). The FeP_2 NWs also have a polycrystalline nature (Fig. 3c). For the single-crystalline domain of FeP and FeP_2, d_{011} = 2.7 Å (at the zone axis of [211]) and d_{110} = 3.7 Å (at the zone axis of [111]) were identified, respectively. The average diameters of FeP and FeP_2 NWs are 60 and 100 nm, respectively. EDX spectra show Fe:P= 1:1 and 1:2, respectively, for FeP and FeP_2 NWs (Fig. 3d).

The sample (1 mg cm^{-2}) was deposited on a GC electrode, and the performance was examined at a rotation speed of 1600 rpm. Table 1 summarizes the current densities (needed to deliver 10 mA cm^{-2}) and Tafel parameters. The FeP and FeP_2 NWs showed Tafel slopes of 66 and 40 mV dec^{-1} in 0.5 M H_2SO_4 and 134 and 100 mV dec^{-1} in 1 M KOH, respectively (Fig. S4, ESI†). The current densities are lower than those of the NW arrays. The chronoamperometric response data indicate that the HER catalytic activity of FeP_2 is more stable than that of FeP over long-term testing (8 h) in both acidic and basic media (Fig. S5, ESI†). The current attenuation of FeP_2 is less than 5 %. Therefore, we concluded that the richer P composition resulted in persistently excellent electrocatalytic efficiency upon cycling.

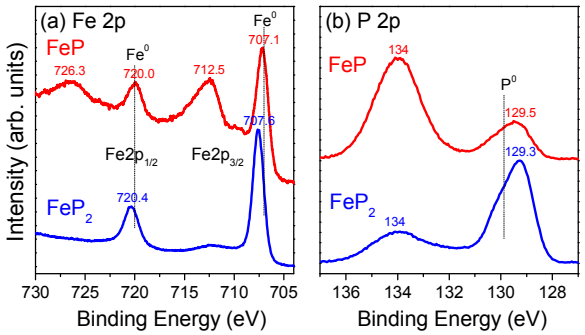

Fig. 4 Fine-scan (a) XPS Fe $2p_{3/2}$ and $2p_{1/2}$ and (b) P $2p$ peaks of FeP and FeP_2 NWs. The position of the neural element peak is marked by a dotted line to clearly delineate the shift.

We performed XPS measurements to investigate the electronic structures. The peak features are virtually the same for both the array and freestanding NWs (see the ESI†, Fig. S6) and are consistent with previous works.[10,12-22] Because the probe depth is a few nm for the photoelectrons of Fe $2p$ and P $2p$, the XPS peaks originate solely from the surface of the FeP and FeP_2 NWs. Fig. 4a shows the Fe $2p_{1/2}$ and $2p_{3/2}$ peaks for FeP and FeP_2 NW arrays. The peaks of neutral Fe at 720.1 and 707.0 eV are indicated. The $2p_{3/2}$ peak of FeP consisted of two bands with peak positions of 707.1 (0.1) and 712.5 (5.5) eV. The value in parentheses represents the blue shift of each band. The first band mainly originated from the Fe-P bonding structures. Referring to the data for FeO (Fe^{2+} at 709 eV) and Fe_2O_3 (Fe^{3+} at 711 eV), the second band is assigned to native (amorphous) oxide layers at the surface, respectively.[41] The negligible blue shift of the Fe-P band indicated the metallic state of Fe. For the FeP_2 NWs, the Fe-P band is observed at 707.6 (0.6), which is more blue shifted than that of FeP. This is because of the increased electron withdrawal resulting from the larger amount of P. Nevertheless, the oxidation number of Fe ions in FeP_2 would be much less than +2. The Fe-O band becomes negligible.

Fig. 4b shows the P $2p$ peaks at 129.5 eV and 129.3 eV for FeP and FeP_2 NWs, respectively, which are red shifted by 0.4 and 0.6 eV from the neutral peak (129.9 eV for $2p_{3/2}$). This band originated from the negatively charged P ions of the P-Fe bonding structures. The larger peak shift observed for the FeP_2 NWs is caused by the larger amount of P, which also causes the relatively large blue shift of the Fe $2p$ Fe-P band. The higher energy peak at 134 eV is ascribed to the P-O bonding structure of (amorphous) oxide forms, such as phosphate. The FeP_2 NWs exhibit a much smaller P-O band than the FeP NWs. It is concluded that as the P content increases, the surface oxidation decreases significantly.

Liu and Rodriguez predicted that Ni_2P could be an excellent

catalyst for HER using density functional theory calculations. They suggested that proton-acceptor (P sites) and hydride-acceptor sites (Ni sites) work in a cooperative manner.[42] The same model can be used to rationalize the FeP and FeP_2 NWs studied here. Both Fe and P are active sites for the HER, functioning as the hydride-acceptor and proton-acceptor centers, respectively. It was expected that Fe ions in FeP, being more metallic than those in FeP_2, became more favorable hydride-acceptor sites. However, more negative charged P anions in FeP_2 created the more active proton-acceptor sites. The higher concentration of the exposed active P ions can also increase the catalytic activity. Furthermore the rich P composition protects more effectively the oxidation of metal ions. This probably explains why the FeP_2 NWs exhibit higher HER catalytic activity than the FeP NWs with a higher stability.

In summary, we synthesized FeP and FeP_2 NW arrays on large substrate areas by reacting pre-grown vertically aligned Fe_2O_3 NWs (on Fe foils) and PH_3. The FeP and FeP_2 NWs exhibit excellent performance for electrocatalytic HER in both strong acidic and basic aqueous solutions. The Tafel slopes are 39 and 37 mV dec^{-1} in 0.5 M H_2SO_4 and 75 and 67 mV dec^{-1} in 1 M KOH, respectively. In addition, we also synthesized freestanding FeP and FeP_2 NWs by phosphidation of pre-grown Fe NWs and found that the Tafel slopes are 66 and 40 mV dec^{-1} in 0.5 M H_2SO_4, respectively. The FeP_2 NWs exhibit higher electrocatalytic efficiency and better durability than the FeP NWs. XPS analysis revealed the more negative charged P anions for FeP_2, which can create the more active proton-acceptor sites. The richer P composition protects effectively the oxidation of metal ions, which promises a higher stability of catalytic activity. Therefore, the FeP_2 NW catalyst that showed excellent performance is a promising material for the development of water-splitting cells able to compete with conventional hydrogen sources.

Notes and references

1 T. F. Jaramillo, K. P. Jørgensen, J. Bonde and J. H. Nielsen, *Science*, 2007, **317**, 100.
2 Y. Li, H. Wang, L. Xie, Y. Liang, G. Hong and H. Dai, *J. Am. Chem. Soc.*, 2011, **133**, 7296.
3 H. I. Karunadasa, E. Montalvo, Y. Sun, M. Majda, J. R. Long and C. J. Chang, *Science*, 2012, **335**, 698.
4 D. Voiry, H. Yamaguchi, J. Li, R. Silva, D. C. B. Alves, T. Fujita, M. Chen, T. Asefa, V. B. Shenoy, G. Eda and M. Chhowalla, *Nat. Mater.*, 2013, **12**, 850.
5 X. Huang, Z. Zeng, S. Bao, M. Wang, X. Qi, Z. Fan and H. Zhang, *Nat. Commun.*, 2013, **4**, 1444.
6 Y. Zheng, Y. Jiao, Y. Zhu, L. H. Li, Y. Han, Y. Chen, A. Du, M. Jaroniec and S. Z. Qiao, *Nat. Commun.*, 2014, **5**, 3783.
7 C. G. Morales-Guio, L. Stern and X. Hu, *Chem. Soc. Rev.*, 2014, **43**, 6555.
8 X. Zou and Y. Zhang, *Chem. Soc. Rev.*, 2015, **44**, 5148.
9 Y. Xu, R. Wu, J. Zhang, Y. Shi and B. Zhang, *Chem. Commun.*, 2013, **49**, 6656.
10 Y. Liang, Q. Liu, A. M. Asiri, X. Sun and Y. Luo, *ACS Catal.*, 2014, **4**, 4065.
11 J. F. Callejas, J. M. McEnaney, C. G. Read, J. C. Crompton, A. J. Biacchi, E. J. Popczun, T. R. Gordon, N. S. Lewis and R. E. Schaak, *ACS Nano*, 2014, **8**, 11101.
12 Z. Zhang, B. Lu, J. Hao, W. Yang and J. Tang, *Chem. Commun.*, 2014, **50**, 11554.
13 P. Jiang, Q. Liu, Y. Liang, J. Tian, A. M. Asiri and X. Sun, *Angew. Chem. Int. Ed.*, 2014, **53**, 12855.
14 R. Liu, S. Gu, H. Du and C. M. Li, *J. Mater. Chem. A*, 2014, **2**, 17263.
15 J. Tian, Q. Liu, Y. Liang, Z. Xing, A. M. Asiri and X. Sun, *ACS Appl. Mater. Interfaces*, 2014, **6**, 20579.
16 J. Jiang, C. Wang, J. Zhang, W. Wang, X. Zhou, B. Pan, K. Tang, J. Zuo and Q. Yang, *J. Mater. Chem. A*, 2015, **3**, 449.
17 S. Han, Y. Feng, F. Zhang, C. Yang, Z. Yao, W. Zhao, F. Qiu, L. Yang, Y. Yao, X. Zhuang and X. Feng, *Adv. Funct. Mater.*, 2015, **25**, 3899.
18 Z. Zhang, J. Hao, W. Yang, B. Lu and J. Tang, *Nanoscale*, 2015, **7**, 4400.
19 Z. Pu, C. Tang and Y. Luo, *Int. J. Hydrogen Energy*, 2015, **40**, 5092.
20 H. Du, S. Gu, R. Liu and C. M. Li, *Int. J. Hydrogen Energy*, 2015, **40**, 14272-14278.
21 X. Yang, A. Y. Lu, Y. Zhu, S. Min, M. N. Hedhili, Y. Han, K. W. Huang and L. J. Li, *Nanoscale,* 2015, **7**, 10974.
22 Y. Yam, B. Y. Xia, X. Ge, Z. Liu, A. Fisher and X. Wang, *Chem. Eur. J.*, 2015, **21**, DOI: 10.1002/chem.201503777.
23 E. J. Popczum, C. G. Read, C. W. Roske, N. S. Lewis and R. E. Schaak, *Angew. Chem. Int. Ed.*, 2014, **53**, 5427.
24 Q. Liu, J. Tian, W. Cui, P. Jiang, N. Cheng, A. M. Asiri and X. Sun, *Angew. Chem. Int. Ed.*, 2014, **126**, 6828.
25 J. Tian, Q. Liu, A. M. Asiri and X. Sun, *J. Am. Chem. Soc.*, 2014, **136**, 7587.
26 Y. Yang, H. Fei, G. Ruan and J. M. Tour, *Adv. Mater.*, 2015, **27**, 3175.
27 J. F. Callejas, C. G. Read, E. J. Popczun, J. M. McEnaney and R. E. Schaak, *Chem. Mater.*, 2015, **27**, 3769.
28 E. J. Popczum, J. R. McKone, C. G. Read, A. J. Biacchi, A. M. Wiltrout, N. S. Lewis and R. E. Schaak, *J. Am. Chem. Soc.*, 2013, **135**, 9267.
29 A. R. J. Kucernak and V. N. N. Sundaram, *J. Mater. Chem. A*, 2014, **2**, 17435.
30 A. B. Laursen, K. R. Patraju, M. J. Whitaker, M. Retuerto, T. Sarkar, N. Yao, K. V. Ramanujachary, M. Greenblatt and G. C. Dismukes, *Energy Environ. Sci.*, 2015, **8**, 1027.
31 Y. Pan, Y. Liu, J. Zhao, K. Yang, J. Liang, D. Liu, W. Hu, D. Liu, Y. Liu, C. Liu, *J. Mater. Chem. A*, 2015, **3**, 1656.
32 X. Wang, Y. V. Kolen'ko, X. Bao, K. Kovnir and L. Liu, *Angew. Chem. Int. Ed.*, 2015, **54**, 8188-8192.
33 M. Ledendecker, S. K. Calderón, C. Papp, H. Steinrück, M. Antonietti and M. Shaldom, *Angew. Chem. Int. Ed.*, 2015, **54**, 12361.
34 J. Tian, Q. Liu, N. Cheng, A. M. Asiri and X. Sun, *Angew. Chem. Int. Ed.*, 2014, **53**, 9577.
35 Z. Xing, Q. Liu, A. M. Asiri and X. Sun, *Adv. Mater.*, 2014, **26**, 5702.
36 X. Chen, D. Wang, Z. Wang, P. Zhou, Z. Wu, F. Jiang, *Chem. Commun.*, 2014, **50**, 11683.
37 J. Kibsgaard and T. F. Jaramillo, *Angew. Chem. Int. Ed.*, 2014, **53**, 14433.
38 T. Wang, K. Du, W. Liu, Z. Zhu, Y. Shao and M. Li, *J. Mater. Chem. A*, 2015, **3**, 4368.
39 P. Xiao, W. Chen, X. Wang, *Adv. Energy Mater.*, 2015, doi:10.1002/aenm.201500985.
40 C. H. Kim, H. J. Chun, D. S. Kim, S. Y. Kim, J. Park, J. Y. Moon, G. Lee, J. Yoon, Y. Jo, M. H. Jung, S. I. Jung and C. J. Lee, *Appl. Phys. Lett*., 2006, **89**, 223103.
41 A. P. Grosvenor, B. A. Kobe, M. C. Biesinger and N. S. McIntyre, *Surf. Interface Anal.*, 2004, **36**, 1564.
42 P. Liu and J. A. Rodriquez, *J. Am. Chem. Soc.*, 2005, **127**, 14871.

Entry for the Table of Contents

Text for Table of Contents

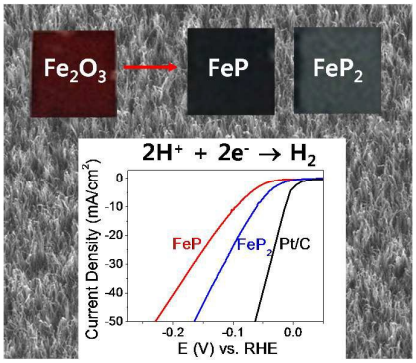

FeP and FeP_2 nanowires exhibit excellent electrocatalytic abilities toward hydrogen evolution from water splitting.